Letter

Ratchetlike motion of helical bilayers induced by boundary constraints

Michio Tanaka,[1,*] Xinyu Wang,[2,1,*] Chandan K. Mishra,[1,3] Jianguo Cai,[2] Jian Feng,[2] Randall D. Kamien,[1] and A. G. Yodh[1]

[1]*Department of Physics and Astronomy, University of Pennsylvania, Philadelphia, Pennsylvania 19104, USA*

[2]*Department of Civil Engineering, Southeast University, Nanjing 210096, China*

[3]*Discipline of Physics, Indian Institute of Technology (IIT) Gandhinagar Palaj, Gandhinagar, Gujarat 382355, India*

(Received 21 September 2021; revised 16 March 2022; accepted 23 June 2022; published 20 July 2022)

We show that application of boundary constraints generates unusual folding behaviors in responsive (swellable) helical bilayer strips. Unlike the smooth folding trajectories typical of free helical bilayers, the boundary-constrained bilayers exhibit intermittent folding behaviors characterized by rapid, steplike movements. We experimentally study bilayer strips as they swell and fold, and we propose a simple model to explain the emergence of ratchetlike behavior. Experiments and model predictions are then compared to simulations, which enable calculation of elastic energy during swelling. We investigate the dependence of this steplike behavior as a function of elastic boundary condition strength, strip length, and strip shape; interestingly, "V-shape" strips with the same boundary conditions fold smoothly.

DOI: 10.1103/PhysRevE.106.L012605

Spontaneous and driven transformation of structured thin films into complex three-dimensional (3D) morphologies has been reported in a wide variety of soft materials [1–8]. These phenomena occur in nature [9–11], and soft materials that exhibit these responsivities hold potential for controlled generation of movements needed in robotics and related applications [12–16]. One important class of soft actuator is based on programed helices. Among various possible shapes, helical structures respond in simple ways and are comparatively easy to fabricate. Moreover, when these twisted structures exhibit discrete helicity changes called perversions, they can be made to bend in specific directions, for example, via tailored topographical patterning [17], layering of aligned filaments [18,19], and orientation of liquid crystal director fields [20,21].

In this contribution, we explore the effects of boundary conditions on the deformation behavior of responsive helical bilayer structures. Specifically, we show how different physical constraints applied to the ends of programed bilayer ribbons can lead to twisting and bending deformation trajectories with "stable" morphological states separated by rapid transitions through "unstable" states. Boundary condition effects on passive helical structures have been noted previously [22–27]. With few exceptions [19,27,28], however, studies of active programed helices have focused on motions with unconstrained or free boundary conditions. Our study reveals that constrained boundary conditions can produce complex, "ratchetlike,"spatiotemporal folding behaviors and force dynamics. Experiment and simulation offer insights for control of actuation with soft thin films. Since soft actuators are often attached at their ends, i.e., constrained by boundary conditions, these insights could be useful for actuation design. Further, this use of mechanical instability and zero net twist to induce many buckling events in succession, without using multiple copies of a simple bistable system, is unique in the field of soft actuators [29].

The essential features of the phenomenon are illustrated in Fig. 1 and Supplemental Material [30] Video S1. We employ swellable bilayer strips with a variety of programed topographies [17] designed to induce helix formation upon swelling. To introduce periodic frustration, the bilayer has a perversion at the strip center with opposite helicity on each side of the perversion [see Fig. 1(b)]. Upon swelling, the strip with constrained boundary conditions exhibits an on-off curling behavior with short time periods, during which single loops are rapidly added and the end-to-end displacement abruptly decreases, and long intervening time periods during which motion largely ceases until the next discrete jump [see Fig. 1(c) and Supplemental Material [30] Video S1]. We describe this motion as "ratchetlike."By contrast, the swelling behavior of a similar bilayer strip, but with free ends, exhibits steady continuous curling and a smooth decrease of end-to-end length; this process begins rapidly and slowly asymptotes to a final morphology (see experiments in Supplemental Material [30] Video S2 and Fig. S1).

The "ratchetlike "motion arises because a discrete set of geometric bilayer configurations permit the strip to satisfy boundary conditions with minimal deformation. We experimentally characterize these boundary condition effects, employing end-to-end displacement vs time measurements as a function of topographic pattern, and boundary condition type. We also carry out numerical simulations of the swellable bilayer strip system wherein we observe similar behavior. Insights from experiment and simulation elucidate the basic effects and suggest ways to design strips with specific sensitivities to boundary conditions, thus offering alternative means to control the dynamics of curling and folding.

[*]These authors contributed equally to this work.

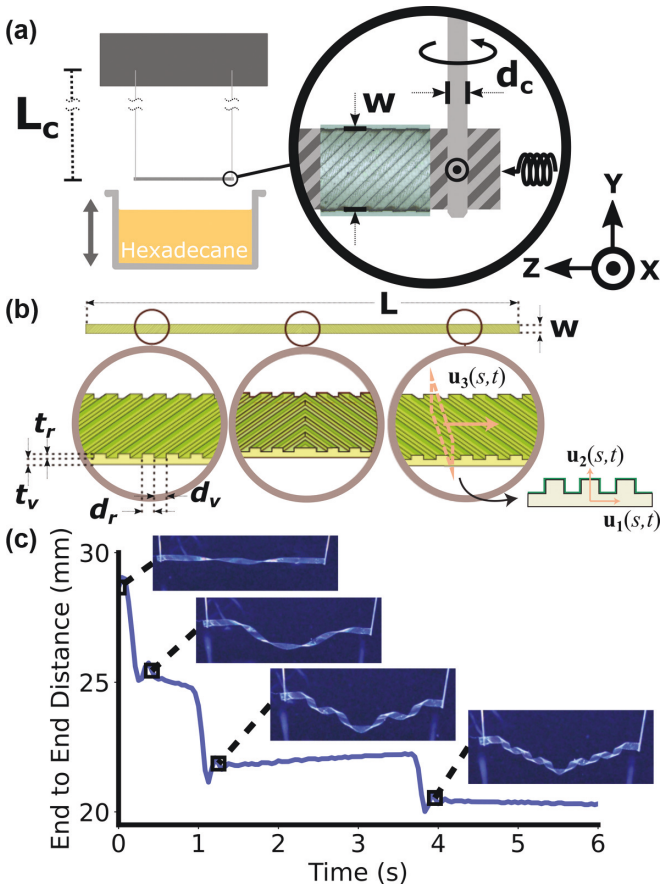

FIG. 1. (a) Illustration of the experimental setup for submerging the swelling of the strip in hexadecane. The setup is shown before the hexadecane bath is moved upwards to submerge the bilayer strip. (Inset) Details of the boundary condition. An experimental image of the strip is included. In practice, $L_c \approx 30$ cm, $d_c \approx 0.25$ mm, and $w = 1$ mm. The thickness of the strip (into the page) is 50 μm. The strip ends are constrained by the metal post; it can rotate about the y axis only, and it can displace along the x and z axes only (subject to an elastic restoring force). (b) Schematic of the strip. $L = 30$ mm, $w = 1$ mm, $t_r \approx t_v \approx 50$ μm, and $d_r = d_v = 100$ μm. Yellow is PDMS; green is parylene. (Left) The local orthonormal basis is depicted. $\mathbf{u_3}(s,t)$ points along the tangent of the strip's centerline, $\mathbf{u_1}(s,t)$ points widthwise, perpendicular to $\mathbf{u_3}$ while remaining in the plane of the strip, and $\mathbf{u_2}(s,t)$ is the remaining orthogonal vector normal to the plane of the strip. (c) Experimental end-to-end displacement vs time plot for the bilayer strip with constrained-rotation elastic boundary conditions. The plot is annotated with experimental images of the strip (contrast is increased for visual clarity). A steplike trajectory of the end-to-end displacement is apparent, indicative of intermittent short bursts of rapid curling activity between quasistable configurations.

The bilayer strips (Supplemental Material [30] Fig. S5) are fabricated primarily by following the topographical patterning scheme outlined in Ref. [17]. The base layer of the strip consists of "soft" crosslinked polymer, polydimethylsiloxane (PDMS) approximately 50 μm thick (with 8-to-1 polymer to crosslinker ratio). For topographic patterning, 50-μm-tall ridges are imprinted into the PDMS (50 μm wide, spaced periodically 50 μm apart). The second, "hard" layer consists of a thin, 1 μm conformal coating of parylene on the patterned side of the PDMS layer.

The enormous difference in elastic moduli and swelling ratio of PDMS and parylene leads to helical deformation of the bilayer film when immersed in hexadecane. In hexadecane, the PDMS layer expands isotropically by roughly 12% [31], but the parylene layer barely expands. The resulting mismatch in strain is relieved by out-of-plane buckling. The topographic pattern, much like the corrugation of a steel roof, induces an anisotropic bending compliance that produces bending exclusively along the axis perpendicular to the ridges. Thus, a rectangular strip with ridges oriented at an angle between 0° and 90° with respect to its long axis will experience uniform bending along an angle to its long axis, which generates the helix configuration.

We introduce periodic *frustration* into the system by patterning the left half of a strip with ridges oriented 45° relative to the long axis and the right half with the mirror image [Fig. 1(b)]. Thus, each half-strip will have opposite handedness when swelled, and a perversion will form at the center. Additionally we made other kinds of strips wherein left- and right-hand sides join at an angle, forming a "V-shape" strip (Supplemental Material [30] Fig. S7) with perversion at the center.

By gluing each end of the bilayer film to long (30 cm) stainless steel posts with 0.25 mm diameter, we introduce rigid boundary conditions at the strip ends. The ends are constrained so that they rotate only along the y axis and so that elastic boundary conditions are produced by the springlike deflection of the posts in response to force along the x and z directions [Fig. 1(a)]. The opposite ends of the posts are spaced to minimize slack in the bilayer film. Importantly, any change in post orientation requires much more torque than the swelling strip can provide; thus, strip rotation at the boundaries is constrained under all experimental conditions.

For swelling-induced deflections (δ_B) that are small compared to the post length (L_c), the ends of the posts deflect linearly with a force, F, according to $\delta_B \propto F L_c^4$ [32]. We define the effective spring constant of the deflection of the posts, K_b, such that $\delta_B = K_b F$. We employ video microscopy to record the strip shape and its end-to-end displacement starting immediately after the strip is submerged in hexadecane. The images are captured at 24 frames per second with a tripod-mounted digital single lens reflex camera (DSLR) and a 55 mm lens. We use a simple image-correlation based tracking algorithm [33] to determine the position of both left and right ends of the strip, starting 0.25 s after the strip is submerged.

When the bilayer film is submerged in hexadecane, strips with free and constrained boundary conditions exhibit very different dynamical behaviors. With free boundary conditions, additional loops are added to the strips on the left and right sides of the perversion via independent motion at the strip ends. This process proceeds at a rate that slowly and smoothly decreases over time until the solvent saturates the soft PDMS layer (Supplemental Material [30] Video S2 and Fig. S1).

By contrast, with constrained boundary conditions, the additional loops are added in a ratcheting fashion, i.e., in rapid motions that punctuate long (∼2 s) durations of relative inactivity. The rapid motions are accompanied by steplike end-to-end length contractions [Fig. 1(c); Supplemental

Material [30] Video S1]. The boundary constraints render some stages of the swelling process more stable than others, which produces long-lived inactive periods.

To extract the strip geometry and deformation energy, we performed simulations in Abaqus/Implicit [34] using geometric and material parameters similar to experiment (for details, see Supplemental Material [30] Sec. S3). From the modeling, we calculate the elastic energy cost for compliance. Specifically, we apply the Kirchhoff Rod Model [35] to our simulation geometries. At each time, t, and for each position along the strip, s, we extract the local orthonormal basis of the strip, $(\mathbf{u_1}(s,t), \mathbf{u_2}(s,t), \mathbf{u_3}(s,t))$; here $\mathbf{u_3}(s,t)$ is aligned with the strip tangent, $\mathbf{u_2}(s,t)$ is normal to the strip, and $\mathbf{u_1}(s,t)$ is the other in-plane basis vector [see Fig. 1(b)]. From this information, we can calculate the vector-valued function, $\boldsymbol{\kappa}(s,t)$, of arc length, s, and time t such that $\frac{d}{ds}\mathbf{u_i}(s,t) = \boldsymbol{\kappa}(s,t) \times \mathbf{u_i}(s,t)$; $\boldsymbol{\kappa}(s,t)$ is the twist vector. The components of the twist vector $\boldsymbol{\kappa}(s,t) = (\kappa_1(s,t), \kappa_2(s,t), \kappa_3(s,t))$ characterize strip shape; note, $\kappa_3(s)$ is commonly labeled $\tau(s)$, the torsion of the curve. For each time t, we calculate the energy, $\mathcal{E}(t)$, of the constrained strip using

$$\mathcal{E}(t) = \int_0^L ds \left\{ \frac{EI_1}{2}[\kappa_1(s,t)]^2 + \frac{EI_2}{2}[\kappa_2(s,t)]^2 + \frac{GJ}{2}[\tau(s,t)]^2 \right\} + W(t). \quad (1)$$

Here E, I_1, I_2, G, J represent the elastic modulus, the two second area moments, the shear modulus and the torsion constant. We determined the values of these constants by fitting Eq. (1) to simulation results. $W(t) = 2\mathbf{F}(t) \cdot \mathbf{u}(L/2, t)$, represents the work done by the strip on the springs at the boundaries [35] (for details, see Supplemental Material [30] Sec. S2).

The simulations exhibit behaviors close to that of the experiments. With free boundary conditions, we observe continuous motion as in experiment (Supplemental Material [30] Video S3 and Fig. 3). Then, after introducing the more rigid boundary conditions, we find that the strip undergoes discrete addition of loops and steplike end-to-end length decrements (Fig. 2 and Supplemental Material [30] Video S4).

We can gain insight about the physics that produces this ratcheting effect by considering the behavior of the unconstrained strip, wherein the curling is continuous and the strip tangents at the strip ends precess during curling. For simplicity, we model the unconstrained strip as two helices of opposite handedness, concatenated such that their center line is continuous [Fig. 3(a)]. Each helix has constant curvature κ and constant torsion τ and fixed length $\frac{L}{2}$; we set $\tau = \kappa$ to account for the 45° bending direction. Consider the two vectors, $\mathbf{e_1}$ and $\mathbf{e_2}$, that represent the unit tangent vectors, respectively, of one end and the other end of the strip. [Note that clamped boundary conditions fix the ends of the strip to have parallel alignment ($\mathbf{e_1} \cdot \mathbf{e_2} = 1$).] Therefore, at each stage in the swelling process, an energy cost $\mathcal{E}_{\text{cost}}$ is incurred to enforce this parallel alignment, and this energy cost increases with departure from parallel alignment, i.e., $E_{\text{cost}} = E_{\text{cost}}(e_1 \cdot e_2)$ strictly decreasing. $\kappa = 0$ corresponds to an unswelled strip, which has completely parallel aligned tangents, ($\mathbf{e_1} \cdot \mathbf{e_2} = 1$) and minimal energy cost. Absent boundary constraints, as κ is increased, the strip ends will lose alignment; $\mathbf{e_1}$ and $\mathbf{e_2}$ will point in different directions at various stages of the swelling process [see Fig. 3(b)]. Therefore, as the strip swells, local elastic energy must be "spent" to keep the tangent vectors in the parallel configuration, satisfying the boundary constraints. These boundary conditions will be satisfied periodically in

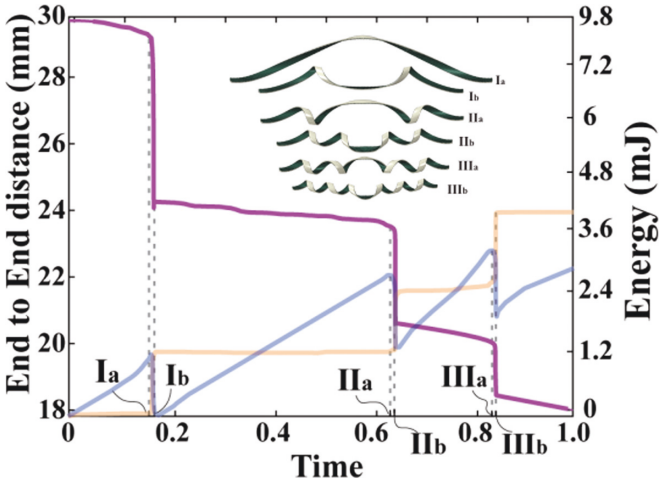

FIG. 2. (Purple line) Simulation of end-to-end displacement vs (normalized) time for the strip with constrained rotation and elastic boundary conditions. Six time points before and after three jumps are noted. (Blue line) Elastic energy vs (normalized) time for the strip with constrained boundary conditions. (Orange line) Work done by the strip on the elastic boundary conditions. (Inset) Simulation images at the six noted times.

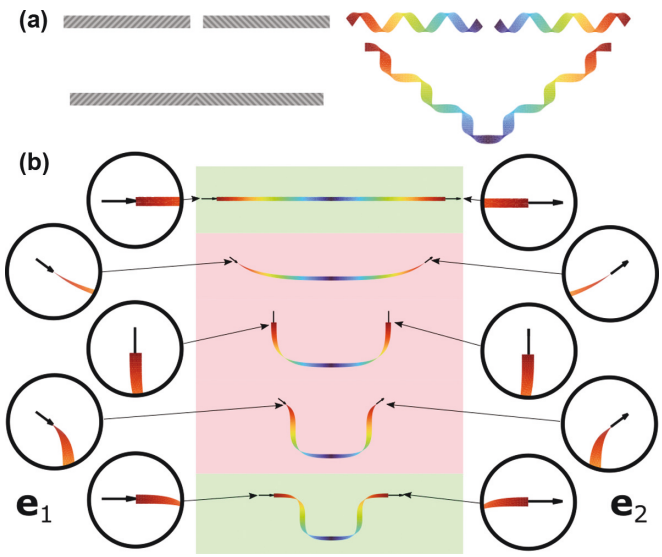

FIG. 3. (a) Schematic of idealized model. The strips consist of concatenated helices of opposite handedness. (b) The "stable," long-lived configurations of the strip, highlighted in green, have parallel (aligned) tangents on both ends. The "unstable" states that are passed through very quickly during the periods of rapid curling activity, highlighted in red, do not have parallel (aligned) tangents; therefore these configurations incur an elastic energy cost to satisfy boundary conditions and are passed over rapidly in transitions between subsequent stable states.

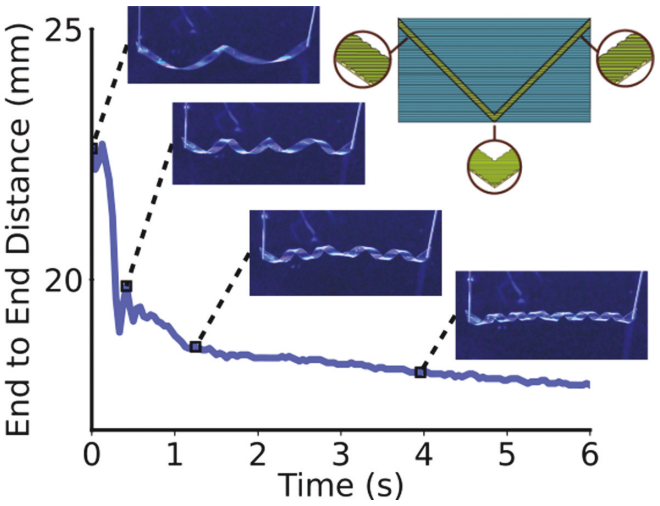

FIG. 4. Experimental end-to-end displacement vs time of the "V-shape" strip with constrained boundary conditions. Notice that, after the initial sharp jump (attributable to slack in the strip), the trajectory of the end-to-end displacement is smooth and absent rapid curling events. (Top right inset) Depiction of the "V-shape" cut used to form the "V-shape" strip.

time as the bilayer film swells, and at these times the most stable configurations are achieved. The observed jumps arise from rapid transitions over energetically unfavorable regions between one stable configuration and the next.

This simple intuitive model also makes predictions about the swelling behavior of strips with other shapes. Consider a strip with "V-shape" geometry (Fig. 4 inset). The "V-shape" strip is cut from a sheet that forms a cylinder when swelled, thus the unit tangent vectors of either end of the strip $\mathbf{e_1}$ and $\mathbf{e_2}$ lie approximately on the axial geodesic of a shrinking cylinder [Supplemental Material [30] Fig. S7(a)]. Accordingly, $\mathbf{e_1} \cdot \mathbf{e_2} \approx 1$ at all times during the swelling process. The strip never incurs a large, periodic energy cost to satisfy the boundary condition, and therefore the "V-shape" strip does not experience the short-lived energetically unfavorable states during swelling. Thus we should not observe rapid ratchetlike transitions through these states; its swelling dynamics should resemble that of the free "straight" strips.

To test this idea, we studied the behavior of the "V-shape" bilayer film. In the experiments, the actuating behavior of "V-shape" bilayer films with free and with applied boundary conditions are similar. The ends of the strip move to facilitate continuous addition of loops in the free case (Supplemental Material [30] Video S5 and Fig. S2), and aside from a single jump at the start of the process, the "V-shape" strip with constrained boundary conditions exhibit continuous curling and end-to-end length contraction (Supplemental Material [30] Video S6 and Fig. 4). This smooth motion contrasts with the discrete, intermittent motion of the "straight" strip with constrained boundary conditions. Similar trends are observed in simulation [Supplemental Material [30] Videos S7 and S8 and Fig. S4 and Fig. S7(b)].

Finally, we explore the dependence of the boundary condition stiffness and strip length on these behaviors. With increasing effective elastic constant of the deflection of the attached boundary posts, K_b, we observe softening of the jumps and a decrease in the number of rapid jumps from three to two, followed by a complete elimination of the jumps (Supplemental Material [30] Fig. S9). Similarly in simulations, increasing the boundary spring constants by two orders of magnitude effectively eliminates the jumps and length contraction when swelled; decreasing spring constants in the simulations by one order of magnitude results in a single "strong" jump (Supplemental Material [30] Fig. S11);. We surmise that when the ends are well constrained, the energy barrier for adding an additional loop becomes very large.

In a different vein, as the strip length is increased, the jumps are spaced more closely in time/length, are greater in number, are of smaller relative magnitude, and are smoother in character (Supplemental Material [30] Fig. S10). For strips with very long lengths, these effects give the impression of a smooth curling process akin to that of the "V-shape" strip. Similar behavior is observed in simulations (Supplemental Material [30] Fig. S12).Conceptually, less deformation per unit length is required to satisfy the boundary conditions for the longer strips, and the effects of frustration are ameliorated.

In summary, we have demonstrated boundary-condition-induced ratchetlike motions of swelling bilayer strips. In both experiment and simulation we observe a folding trajectory punctuated by discrete periods of rapid activity when the boundaries are constrained and a continuous folding trajectory under free boundary conditions. These general concepts can be applied to understand other active deformable structures with boundary constraints, as well as to create conditions for active sheets of soft material that produce vigorous steplike movement.

We thank H. Xiao for technical assistance, as well as Joonwoo Jeong, Shu Yang, P. J. Collings, and Ajay Sood for consultation and advice. This work was supported by the NSF (DMR2003659) and the PENN MRSEC (DMR1720530) including its Optical Microscopy Shared Experimental Facility. Some of this work was carried out at the Singh Center for Nanotechnology, which is supported by the NSF National Nanotechnology Coordinated Infrastructure Program under grant NNCI-2025608. R.D.K. was supported by a Simons Investigator under Grant No. 291825 from the Simons Foundation.

[1] L. Zhang, I. Desta, and P. Naumov, Synergistic action of thermoresponsive and hygroresponsive elements elicits rapid and directional response of a bilayer actuator, Chem. Commun. **52**, 5920 (2016).

[2] N. Bassik, B. T. Abebe, K. E. Laflin, and D. H. Gracias, Photolithographically patterned smart hydrogel based bilayer actuators, Polymer **51**, 6093 (2010).

[3] Y. Cheng, K. Ren, D. Yang, and J. Wei, Bilayer-type fluorescence hydrogels with intelligent response serve as temperature/pH driven soft actuators, Sensors Actuators B **255**, 3117 (2018).

[4] D. E. Hagaman, S. Leist, J. Zhou, and H.-F. Ji, Photoactivated polymeric bilayer actuators fabricated via 3D printing, ACS Appl. Mater. Interfaces **10**, 27308 (2018).

[5] D. Kim, H. S. Lee, and J. Yoon, Highly bendable bilayer-type photo-actuators comprising of reduced graphene oxide dispersed in hydrogels, Sci. Rep. **6**, 20921 (2016).

[6] Y. Hu, J. Liu, L. Chang, L. Yang, A. Xu, K. Qi, P. Lu, G. Wu, W. Chen, and Y. Wu, Electrically and sunlight-driven actuator with versatile biomimetic motions based on rolled carbon nanotube bilayer composite, Adv. Funct. Mater. **27**, 1704388 (2017).

[7] W. Sang, L. Zhao, R. Tang, Y. Wu, C. Zhu, and J. Liu, Electrothermal actuator on graphene bilayer film, Macromol. Mater. Eng. **302**, 1700239 (2017).

[8] M. Dai, O. T. Picot, J. M. N. Verjans, L. T. de Haan, A. P. H. J. Schenning, T. Peijs, and C. W. M. Bastiaansen, Humidity-responsive bilayer actuators based on a liquid-crystalline polymer network, ACS Appl. Mater. Interfaces **5**, 4945 (2013).

[9] J. Zheng, P. Xiao, X. Le, W. Lu, P. Théato, C. Ma, B. Du, J. Zhang, Y. Huang, and T. Chen, Mimosa inspired bilayer hydrogel actuator functioning in multi-environments, J. Mater. Chem. C **6**, 1320 (2018).

[10] L. Zhang, S. Chizhik, Y. Wen, and P. Naumov, Directed motility of hygroresponsive biomimetic actuators, Adv. Funct. Mater. **26**, 1040 (2016).

[11] J. Ha, S. M. Choi, B. Shin, M. Lee, W. Jung, and H.-Y. Kim, Hygroresponsive coiling of seed awns and soft actuators, Extreme Mech. Lett. **38**, 100746 (2020).

[12] X. Wang, N. Jiao, S. Tung, and L. Liu, Photoresponsive graphene composite bilayer actuator for soft robots, ACS Appl. Mater. Interfaces **11**, 30290 (2019).

[13] S. Shian, K. Bertoldi, and D. R. Clarke, Dielectric elastomer based "grippers" for soft robotics, Adv. Mater. **27**, 6814 (2015).

[14] S. Wang, Y. Gao, A. Wei, P. Xiao, Y. Liang, W. Lu, C. Chen, C. Zhang, G. Yang, H. Yao *et al.*, Asymmetric elastoplasticity of stacked graphene assembly actualizes programmable untethered soft robotics, Nat. Commun. **11**, 4359 (2020).

[15] H. Kim, H. Lee, I. Ha, J. Jung, P. Won, H. Cho, J. Yeo, S. Hong, S. Han, J. Kwon *et al.*, Biomimetic color changing anisotropic soft actuators with integrated metal nanowire percolation network transparent heaters for soft robotics, Adv. Funct. Mater. **28**, 1801847 (2018).

[16] Y. Lee, W. J. Song, and J. Y. Sun, Hydrogel soft robotics, Mater. Today Phys. **15**, 100258 (2020).

[17] J. Jeong, Y. Cho, S. Y. Lee, X. Gong, R. D. Kamien, S. Yang, and A. G. Yodh, Topography-guided buckling of swollen polymer bilayer films into three-dimensional structures, Soft Matter **13**, 956 (2017).

[18] S.-J. Jeon and R. C. Hayward, Reconfigurable microscale frameworks from concatenated helices with controlled chirality, Adv. Mater. **29**, 1606111 (2017).

[19] W. Wang, C. Li, M. Cho, and S.-H. Ahn, Soft tendril-inspired grippers: Shape morphing of programmable polymer–paper bilayer composites, ACS Appl. Mater. Interfaces **10**, 10419 (2018).

[20] J. M. Boothby and T. H. Ware, Dual-responsive, shape-switching bilayers enabled by liquid crystal elastomers, Soft Matter **13**, 4349 (2017).

[21] R. C. P. Verpaalen, M. G. Debije, C. W. M. Bastiaansen, H. Halilović, T. A. P. Engels, and A. P. H. J. Schenning, Programmable helical twisting in oriented humidity-responsive bilayer films generated by spray-coating of a chiral nematic liquid crystal, J. Mater. Chem. A **6**, 17724 (2018).

[22] J. Liu, J. Huang, T. Su, K. Bertoldi, and D. R. Clarke, Structural transition from helices to hemihelices, PLoS ONE **9**, e93183 (2014).

[23] S. Liu, Z. Yao, K. Chiou, S. I. Stupp, and M. Olvera de la Cruz, Emergent perversions in the buckling of heterogeneous elastic strips, Proc. Natl. Acad. Sci. USA **113**, 7100 (2016).

[24] S. J. Gerbode, J. R. Puzey, A. G. McCormick, and L. Mahadevan, How the cucumber tendril coils and overwinds, Science **337**, 1087 (2012).

[25] P. Pieranski, J. Baranska, and A. Skjeltorp, Tendril perversion—A physical implication of the topological conservation law, Eur. J. Phys. **25**, 613 (2004).

[26] A. Ghatak and L. Mahadevan, Solenoids and Plectonemes in Stretched and Twisted Elastomeric Filaments, Phys. Rev. Lett. **95**, 057801 (2005).

[27] N. Charles, M. Gazzola, and L. Mahadevan, Topology, Geometry, and Mechanics of Strongly Stretched and Twisted Filaments: Solenoids, Plectonemes, and Artificial Muscle Fibers, Phys. Rev. Lett. **123**, 208003 (2019).

[28] P. E. S. Silva, J. L. Trigueiros, A. C. Trindade, R. Simoes, R. G. Dias, M. H. Godinho, and F. V. de Abreu, Perversions with a twist, Sci. Rep. **6**, 23413 (2016).

[29] A. Pal, V. Restrepo, D. Goswami, and R. V. Martinez, Exploiting mechanical instabilities in soft robotics: Control, sensing, and actuation, Adv. Mater. **33**, 2006939 (2021).

[30] See Supplemental Material at http://link.aps.org/supplemental/10.1103/PhysRevE.106.L012605 for videos of experiments and simulations, figures of end-to-end displacement vs time, and discussion of simulation details, simulation energy calculation, and model parameters.

[31] The maximum expansion used in simulations was 14%. As the simulations did not take into account dynamics, this resulted in the simulation of a few extra frames after the third jump.

[32] J. M. Gere and B. J. Goodno, *Mechanics of Materials*, 8th ed. (Cengage Learning, Stamford, CT, 2012).

[33] Y. Cheng, Mean shift, mode seeking, and clustering, IEEE Trans. Pattern Anal. Mach. Intell. **17**, 790 (1995).

[34] Dassault Systemes (2017), Abaqus, Retrieve from https://www.3ds.com/products-services/simulia/products/abaqus/ (accessed on January 2017).

[35] B. Audoly and Y. Pomeau, *Elasticity and Geometry: From Hair Curls to the Non-linear Response of Shells* (Oxford University Press, New York, 2018).